



HAL
open science

Ethanol Electro-oxidation on Palladium Revisited Using Polarization Modulation Infrared Reflection Absorption Spectroscopy (PM-IRRAS) and Density Functional Theory (DFT): Why Is It Difficult To Break the C–C Bond?

Evans A. Monyoncho, Stephan N. Steinmann, Carine Michel, Elena A. Baranova, Tom K. Woo, Philippe Sautet

► To cite this version:

Evans A. Monyoncho, Stephan N. Steinmann, Carine Michel, Elena A. Baranova, Tom K. Woo, et al.. Ethanol Electro-oxidation on Palladium Revisited Using Polarization Modulation Infrared Reflection Absorption Spectroscopy (PM-IRRAS) and Density Functional Theory (DFT): Why Is It Difficult To Break the C–C Bond?. ACS Catalysis, 2016, 2016 (6), pp.4894–4906. 10.1021/acscatal.6b00289 . hal-01343876

HAL Id: hal-01343876

<https://hal.science/hal-01343876>

Submitted on 5 Dec 2018

HAL is a multi-disciplinary open access archive for the deposit and dissemination of scientific research documents, whether they are published or not. The documents may come from teaching and research institutions in France or abroad, or from public or private research centers.

L'archive ouverte pluridisciplinaire **HAL**, est destinée au dépôt et à la diffusion de documents scientifiques de niveau recherche, publiés ou non, émanant des établissements d'enseignement et de recherche français ou étrangers, des laboratoires publics ou privés.

Ethanol Electrooxidation on Palladium Revisited using PM-IRRAS and DFT: Why is it difficult to break the C – C bond?

Evans A. Monyoncho,^{a,b} Stephan N. Steinmann,^c Carine Michel,^c Elena A. Baranova,^{b} Tom K. Woo,^a
and Philippe Sautet.^{c*}*

^aDepartment of Chemistry and Biomolecular Sciences, Center for Catalysis Research and Innovation
(CCRI), University of Ottawa, 10 Marie-Curie Private, Ottawa, Ontario K1N 6N5, Canada

^bDepartment of Chemical and Biological Engineering, (CCRI), University of Ottawa, 161 Louis-Pasteur
St., Ottawa, Ontario K1N 6N5, Canada

^cUniv Lyon, ENS de Lyon, CNRS, Université Lyon 1, Laboratoire de Chimie UMR 5182, F-69342,
Lyon, France

Abstract

Insights into ethanol electrooxidation reaction mechanism on palladium in alkaline media are presented combining polarization modulation infrared reflection absorption spectroscopy (PM-IRRAS) and density functional theory (DFT) calculations. The synergy between PM-IRRAS and DFT calculations helps to explain why the C – C bond is not broken during ethanol electrooxidation, and the reaction

stops at acetate. Coupling chronoamperometry (CA) with *in-situ* PM-IRRAS enabled us to simultaneously identify ethanol electrooxidation products on the catalyst surface and in the bulk solution. We show that at lower potential it is possible to break the C – C bond on Pd/C in alkaline media to form CO₂. However, the selectivity is poor due to competition towards the formation of acetate and other side products, which gets worse at higher potentials. DFT calculations were used to complete the picture using the computational hydrogen electrode approach. The calculations highlight the pivotal role of the CH₃CO intermediate that can either undergo a C – C bond scission yielding CO and then CO₂ or that can be oxidized towards CH₃COO⁻. The latter is a dead end in the reaction scheme towards CO₂ production, since it cannot be easily oxidized nor broken into C₁ fragments. CH₃CO is however not the most favored intermediate formed from ethanol electrooxidation on Pd, hence limiting the production of CO₂.

Keywords: Ethanol electrooxidation, Palladium, Spectroelectrochemistry, direct ethanol fuel cells, DFT, computational hydrogen electrode

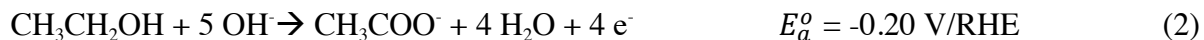
1 Introduction

Fuel cells represent a promising technology for clean power generation because they convert chemical energy (fuel) into electrical energy with high efficiency and low-to-none emission of pollutants.¹⁻⁴ Direct ethanol fuel cells (DEFCs) have several advantages compared to the most studied hydrogen and methanol fuel cells. First and foremost, ethanol is a non-toxic liquid, which lowers the investment of handling facilities because the current infrastructure for gasoline can be largely used.^{5,6} Second, ethanol can be conveniently produced from biomass, hence is carbon neutral which mitigates increasing atmospheric CO₂. Last but not least, if completely oxidized to CO₂, ethanol has a higher energy density

than methanol since it can deliver 12 electrons per molecule following the anodic reaction in equation (1):⁵



In a DEFC, equation (1) is counterbalanced at the cathode by the oxygen reduction reaction, generating a theoretical cell voltage of 1.14 V. However, in practice ethanol is known to be partially oxidized to acetic acid (acetate in alkaline media) giving a maximum of 4 electrons as shown in equation (2):



The almost exclusive oxidation to acetic acid overshadows the attractiveness of DEFC considerably, as the energy density is divided by 3. The standard potential of acetic acid formation indicates that a reaction path including acetic acid, leads to inevitable potential losses of about 0.4 V (difference between ideal potential for CO₂ and acetic acid "production").⁷

The development of alkaline fuel cells has mainly been hampered by the lack of stable and efficient anion exchange membranes. However, this challenge has been well tackled in recent years,^{8,9,9} allowing the development of alkaline fuel cells (AFCs) which are of particular technological interest due to their simple designs and ability to operate at low temperatures (25-100 °C). In alkaline conditions, the kinetic of both the cathodic oxygen reduction and the anodic ethanol oxidation is facilitated. Furthermore, the expensive Pt catalyst can be replaced by the lower-cost and more active transition metals, for instance Pd.¹⁰⁻¹⁴

Therefore, to overcome the limitation of incomplete oxidation of ethanol to CO₂, several studies have attempted to provide a better understanding of the ethanol oxidation on Pd-based catalysts using the previous extensive work on the ethanol oxidation on Pt-based catalysts in acidic conditions as a starting point. Although the detailed understanding of ethanol electrooxidation mechanism is complex and

controversial, there is a general consensus on Pt-based catalysts in acidic conditions that the reaction exhibits the so-called “dual pathway mechanism”^{15,16} or “consecutive-parallel mechanism”.¹⁷ According to this dual path reaction scheme, two major pathways are in competition. In the C₂ pathway, the C – C bond does not break and ethanol is oxidized successively to acetaldehyde and then to acetic acid (acetate in alkaline). In the C₁ pathway, the C – C bond is broken, thus generating C₁ fragments. These fragments are oxidized into CO and eventually CO₂. When shifting to alkaline conditions, very few studies provide detailed molecular information.^{18–23} Christensen *et al.* have shown in several studies that the interfacial pH drops at higher potentials due to the OH⁻ consumption that is not completely counterbalanced by the OH⁻ diffusion from the bulk to the interfacial region.^{22–24} This phenomenon leads to a transition from alkaline to effectively acidic conditions. The transition potential varies with the diffusion rate of OH⁻, i.e., working temperature, flow-rate and so on. They report that during electrooxidation reaction, ethanol is converted to acetate in alkaline pH while above the transition potential, i.e., in pseudo-acidic conditions, it yields acetic acid and trace amounts of CO₂ as a result of the slow C – C bond splitting.²⁵ This is in agreement with the results from online mass-spectrometry, evidencing CO₂ production over Pt and Pd in 0.01 M NaOH, where acetic acid formation is almost absent.²⁶

On Pd-based electrocatalysts, ethanol oxidation reactivity differs compared to Pt, which is illustrated most clearly in acidic conditions, where Pt yields mainly acetic acid and even some CO₂, while Pd is completely inactive.²⁷ In alkaline conditions, Pd is more active and it is generally proposed that ethanol is dehydrogenated into adsorbed acetyl (CH₃CO) (sometimes erroneously called ethoxy) which is further oxidized to acetate by the hydroxyl (OH⁻) species.²⁸ This mechanism has received further credence using *in-situ* attenuated total reflection surface-enhanced infrared absorption spectroscopy (ATR-SEIRAS) measurements.¹⁹ Yang *et al.* reported that ethanol oxidation starts with the α-C – H bond

scission yielding adsorbed CH_3CO as a pivotal intermediate, which may be further oxidized into acetate or, given enough time, would fragment into C_1 adsorbed intermediates (due to observation of adsorbed CO).¹⁹ These observations can be rationalized by recalling that the oxidation of acetyl to acetate is an electrochemical step, and therefore favored by oxidative potentials, while the C – C bond cleavage is expected to be only weakly affected by the potential, assuming that this process is not coupled with an electrochemical step such as the C-OH bond formation.

To complement the experimental insights, modeling studies are also being reported. However, the complexity of the Pd/alkaline electrochemical interface not only challenges experiments but also the atomistic modeling of the underlying mechanism.²⁹ The main ingredients are the electrolyte and its pH, both influencing the reactivity directly (state of the electrode surface) and indirectly (modifying the environment). The electrochemical potential and the inclusion of well-established equilibria, such as the reactivity of acetaldehyde (e.g., enol and aldol formation) or of CO , which can be hydrated to yield formic acid adds to the complexity of the reaction network. It is currently impossible to consider all these aspects on a consistent level in one, exhaustive, study. Furthermore, the size of the "straight forward" reaction network for ethanol oxidation already includes 128 potential C_2 and 21 C_1 intermediates.

The influence of co-adsorbed species and of explicit water molecules has intrigued several groups. In particular, Neurock and co-workers have modeled ethanol oxidation by O_2 in alkaline conditions by including the aqueous media explicitly and adsorbed hydroxyl on the Pd surface.³⁰ They have shown that most of the C – H and O – H scissions of the ethanol oxidation network towards acetic acid/acetate have lower barriers when assisted by co-adsorbed hydroxyl on Pd(111) compared with the bare metal. According to their results, acetaldehyde is a first intermediate towards acetic acid. Then, two possibilities exist: (i) the geminal diol, which can be formed by hydration of the acetaldehyde in

solution, leads straightforwardly to acetic acid (ii) acetaldehyde is either oxidized by the direct formation of a C – OH bond, or the α -C – H bond is broken, leading to acetyl CH_3CO . In a more recent study, Hu and coworkers revisited this mechanism in the electrochemical context, but without accounting for the electrochemical potential. Their conclusions are in line with the ones of Neurock regarding the oxidation by oxygen using a more advanced description of the structure of the water solvent.³¹ It should be noted that under electrochemical conditions, surface OH is also formed in acidic conditions, provided the electrochemical potential is sufficiently positive.³² As a consequence, these simulations can be applied to both alkaline and acidic conditions.

In order to complement these studies, one should include the effect of the electrochemical potential. The electrochemical potential can be included at various levels of sophistication. The most important effects are due to a change in thermodynamics when electrons and protons are exchanged. This effect can be easily obtained as *a posteriori* correction to *ab initio* energies (typically periodic DFT) as originally proposed by Norskov, known as the computational hydrogen electrode.⁷ This approach has been used successfully for MeOH oxidation on a large range of metals^{33–35} and includes the thermodynamic driving force of the (H^+ , OH^-) recombination into H_2O . Several groups have also proposed strategies to include the influence of the potential in the electronic structure computations.^{36–41} Although more accurate, these approaches are also computationally more costly since they require the inclusion of the electrolyte to mimic adequately the capacitance of the interface, either with a continuum model,⁴² a Poisson-Boltzmann theory,^{40,43} or an explicit, but static description.⁴⁴ These approaches have been used for the study of small reaction path networks such as the CO_2 hydrogenation to formic acid⁴⁵ in combination with continuum models for the solvent or methanol and CO oxidation at a Pt catalyst.^{46,47}

The aim of this work is to provide insights as to why the C – C bond is not broken during ethanol electrooxidation and to propose a detailed mechanistic schematic, which can be applied in understanding

experimental observations. Ethanol oxidation potentials were determined by cyclic voltammetry (CV). Chronoamperometry (CA), coupled with *in-situ* polarization modulation infrared reflection absorption spectroscopy (PM-IRRAS), was used to identify the oxidation products both on the catalyst surface and in the bulk solution. Density functional theory (DFT) calculations are exploited to explore all possible intermediates including the electrochemical potential using the computational hydrogen electrode at an alkaline pH of 14. This setup allows us to include the thermodynamic effect of the involvement of hydroxide ions in the reaction mechanism without explicitly co-adsorbing OH on the catalyst surface. The potential energy profiles of the reactions were used to determine the most likely reaction pathway towards acetate on two different facets, Pd(111) and Pd(100). On the most active facet, a complete study of the C₂ and C₁ intermediates was done on the full range of the 12 electron oxidation (from ethanol to CO₂) to select the key intermediates for the C – C bond breaking. Besides, for the first time to the best of our knowledge, we assess the C – C bond breaking from these key intermediates in the context of electro-oxidation. The energy barriers provide general strategies for improving the catalyst towards C – C bond scission.

2 Experimental and computational methods

2.1 Palladium nanoparticles synthesis and characterization

The Pd/C nanoparticles (NPs) were prepared using a polyol method reported in literature.^{48,49} In the synthesis, 0.25 g of anhydrous Palladium chloride (*Fisher*) was dissolved in 50 mL of ethylene glycol (EG) (*Fisher*) and the pH was adjusted to 8 by adding 0.06 M NaOH in EG. The solution was then refluxed at 160° for 2 hours to form nanoparticles. To the resulting colloids, the appropriate amount of carbon black (Vulcan XC – 72 *Cabot, Corp.*) was added to obtain supported catalysts of 20 wt% loading. The mixture was stirred for 48 hours to achieve high dispersion of nanoparticles in carbon. The

supported catalyst was thoroughly washed with de-ionized water (18 Ω cm) to remove EG and salt ions through vacuum filtration and air dried at 100 °C for 4 hours.

The details of physicochemical characterization techniques have been reported in the previous publication.⁴⁹ In summary, the following techniques were used: The High-Angle Annular dark-field (HAADF) scanning transmission electron microscopy (STEM). The FEI Titan3 80-300 microscope model equipped with a CEOS aberration corrector for the probe forming lens and a monochromatic field-emission gun was used. X-ray diffraction pattern (XRD) was collected using a Rigaku Ultima IV diffractometer using a Cu K α X-ray source ($\lambda = 1.54183$ Å, 40 kV, 44 mA). X-ray photoelectron spectroscopy (XPS) measurements were performed in a KRATOS Axis Ultra DLD with a Hybrid lens mode at 140 W and pass energy of 20 eV using a monochromatic Al K α .

2.2 Spectroelectrochemical measurements

All experiments were conducted at room temperature in a customized *in-situ* cell made of Teflon equipped with a hemi-cylinder CaF₂ window (RJ Spectroscopy Co.). A glassy carbon (GC) electrode of 0.1962 cm² geometric surface area was used as the current collector for carbon supported Pd NPs. All potentials were measured with respect to mercury-mercury oxide (Hg/HgO) (Koslow scientific) but reported versus the reversible hydrogen electrode ($E_{(RHE)} = E_{(Hg/HgO)} + 0.855$ vs RHE), unless otherwise stated. A Pt wire served as a counter electrode. 1M (KOH + C₂H₅OH) was used as the electrolyte and was continuously purged with nitrogen gas. The catalyst ink was prepared by dispersing 6 mg of Pd/C powder in 1 ml of de-ionized water, 200 μ L of isopropanol, and 100 μ L of Nafion solution. The mixture was sonicated for 10 min to form a homogeneous mixture. The ink solution (10 μ L) was deposited onto the GC-electrode surface and air dried at room temperature for 15 min and used as the working electrode.

The PM-IRRAS measurements were performed using a Bruker Tensor 37 spectrometer equipped with an external Polarization Modulation Accessory (PMA 50 XL), nitrogen cooled mercury cadmium telluride detector (LN-MCT Narrow PMA50, Infrared Associates Inc., Stuart, FL), photoelastic modulator (PEM-100 controller with II/ZS50 ZnSe, 50 kHz optical head, Hinds Instruments, Hillsboro, OR), and a demodulator [Synchronous Sampling demodulator (SSD), GWC Instruments, Madison, WI]. Electrode potential was controlled by a BioLogic VSP potentiostat equipped with the EC-Lab software (BioLogic Science Instruments SAS, Claix, France). The cell and PMA-50 XL chamber were thoroughly purged with nitrogen gas to remove background atmospheric CO₂ and water vapour. Although the electrolyte was degassed with N₂ before being introduced into the cell, it was degassed for 30 minutes once assembled in the optical path, and then the electrode was pushed against the CaF₂ window without stopping the gas flow. The thin-cavity obtained was wedged in form but the average thickness was estimated⁵⁰ to be 10 μm. Background spectra were collected to track the level of CO₂ in the system. Typically, after two hours the reference spectrum was acquired at the open circuit potential (OCP) followed by sample spectra at various ethanol oxidation potentials selected from the cyclic voltammetry (CV) profile. Sample spectra were acquired under chronoamperometry (CA) conditions at five minutes increments i.e. while holding the potential constant for up to 30 minutes before stepping to another potential.

The signal was acquired by co-addition of 256 interferograms (128 forward and 128 backward scans) collected with a resolution of 8 cm⁻¹. With PM-IRRAS, we are able to simultaneously measure the average reflectivity [$R_{\text{avg}} = (R_p + R_s)/2$] and the difference reflectivity [$R_{\text{dif}} = (R_p - R_s)$] channel with a single detector because of its double-modulation scheme.⁵¹ The R_p and R_s are the reflectivities for p- and s-polarized light, respectively. Although this property comes with many advantages it presents a challenge in processing and interpretation of the data obtained. However, we have recently developed an approach

to overcome this challenge which significantly simplifies PM-IRRAS data interpretation. The details for data processing are presented in the supporting information under “PM-IRRAS Data Processing and Interpretation” which will also be published later together with the detailed experimental optimization procedures in a manuscript currently under preparation (“*Polarization Modulation Infrared Reflection Absorption Spectroscopy (PM-IRRAS) Utility in Electrocatalysis: Experimental and Data Processing Details*” by Evans A. Monyoncho, Vlad Zamlynny, Tom K. Woo, and Elena A. Baranova) In summary, the approach yields strong signal-to-noise ratio enabling us to see weak absorption bands with a very few scans (16 - 256). The approach also allows direct interpretation of the spectra, and gives more insights of the substrate-film system or the reaction mechanism. The signal is reported as absorbance (A) using equation 3 and 4 which corresponds to surface and bulk-solution species, respectively.

$$A = \log \left(\frac{\text{Sample } (R_{dif})}{\text{Reference } s (R_{dif})} \right) \quad \text{vs cm}^{-1} \quad 3$$

$$A = \log \left(\frac{\text{Sample } R_{avg}}{\text{Reference } s (R_{avg})} \right) \quad \text{vs cm}^{-1} \quad 4$$

With this definition, the positive and negative bands in the spectra correspond to species produced or consumed at the sampling potential, respectively with respect to the reference spectrum.

2.3 Computational methods

Density functional theory (DFT) calculations were performed with the Vienna *Ab-initio* Simulation Package (VASP version 5.3.3).^{52,53} The generalized gradient approximation of Perdew, Burke, and Erzenhorf (PBE)⁵⁴ was used to compute the exchange-correlation energy. The projected augmented wave (PAW) method^{55,56} was employed to describe the core-electron interaction. A plane-wave basis set with an energy cut-off was set to 400 eV was used. The Pd surfaces were modeled by a periodic slab with a p(3x3) unit cell of five Pd layers and a vacuum regions of 10 Å. A 7x7x1 Monkhorst-Pack *k*-points mesh was employed for the Brillouin zone integration together with a second order Methfessel-

Paxton smearing method⁵⁷ with a sigma of 0.2 eV. Slabs were cut from the optimized Pd bulk unit cell with a lattice constant of $a = 3.94 \text{ \AA}$ which overestimates the experimental value of 3.89 \AA by 1%. In all geometry optimizations only the top-two Pd monolayers were allowed to relax whereas the bottom three monolayers were kept fixed. All optimizations were carried out to forces below 0.02 eV/\AA .

All energies are referenced to the bare Pd slab, ethanol, water and hydrogen in the gas phase. The latter two serve to introduce oxygen atoms and to account for the coupled proton-electron transfers, respectively. In particular, the reaction energies of electrochemical steps (i.e. steps where the number of protons in the system is changing) are computed according to the computational hydrogen electrode,⁷ e.g. the reaction:



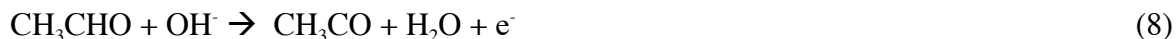
is computed as

$$E_{\text{rxn}} = E_{(\text{CH}_3\text{COOH})} - [E_{(\text{CH}_3\text{CO})} + E_{(\text{H}_2\text{O})} + 0.5 E_{(\text{H}_2)} + U] \quad (6)$$

Where we have assumed U to be with respect to the pH insensitive RHE and a pH of 0. Note that at pH = 14, we write the same expression for the reaction energy, but formulate the reaction as



Similarly, we write



in alkaline conditions and compute the reaction energy (E_{rxn}) as

$$E_{\text{rxn}} = E_{(\text{CH}_3\text{CO})} - [E_{(\text{CH}_3\text{CHO})} + 0.5 * E_{(\text{H}_2)} + U] \quad (9)$$

The transition states (TS) have been located as follows: the state with the C – C bond broken was constructed in analogy to the adsorption mode of the individual fragments. This co-adsorbed state was optimized in order to ensure that no significant lateral interactions were introduced. Then, a rough nudged-elastic band (NEB)⁵⁸ computation with 8 images between the initial and final state was

performed, seeded by interpolations between the two states obtained by Opt'n Path code⁵⁹ which uses a combination of internal and Cartesian coordinates. After about 50 cycles of NEB, an improved guess for the transition state was obtained, which was refined by the dimer method⁶⁰ and verified to be a first order saddle point by a frequency analysis.

Infrared spectra of surface species were modeled following the same procedure, the intensities being evaluated using density functional perturbation theory.⁶¹ Infrared spectra of solution species were computed using the same DFT functional (PBE) combined with a continuum model for the water solvent (PCM)⁶² with a def2-TZVP basis set using the Gaussian09 version D.01 program.⁶³

3 Results and discussion

3.1 Pd/C Nanoparticles characterization and electrochemical performance

The physical, structural, and chemical characterizations of Pd/C are shown in Figure S1; other details have been published elsewhere.⁴⁹ In summary, the supported particle size was determined to be on average 4 ± 2 nm. The XRD pattern showed that the nanoparticles retained the face-centered-cubic (fcc) structure of bulk Pd with peaks at 40, 46 and $68^\circ 2\theta$ corresponding to (111), (200) and (220) reflections, respectively.

Cyclic voltammetry was used to determine ethanol oxidation current/potential profiles for Pd/C nanoparticles in alkaline conditions as shown in Figure 1b. Figure 1b shows a representative CV of Pd/C nanoparticles in 1M (KOH + CH₃CH₂OH) and 1M (KOH + CH₃COOH) solutions at 5 mV s⁻¹. The slow scanning rate helps to capture the oxidation profile with current densities close to a steady-state condition. For ethanol profile, during the *anodic* scan, a positive current starts at 0.39 V and increases *gradually* to a maximum current density at 0.77 V, and then decreases to zero at 1.00 V. During the *cathodic* scan, a positive current was obtained starting at 0.76 V, which increases *rapidly* to a maximum

at 0.66 V, and then decreases to zero at 0.39 V. The CV profile for acetic acid did not show any oxidation current densities, a prove that the resulting acetate ($\text{KOH} + \text{CH}_3\text{COOH}$) is the dead end during ethanol electrooxidation reaction.

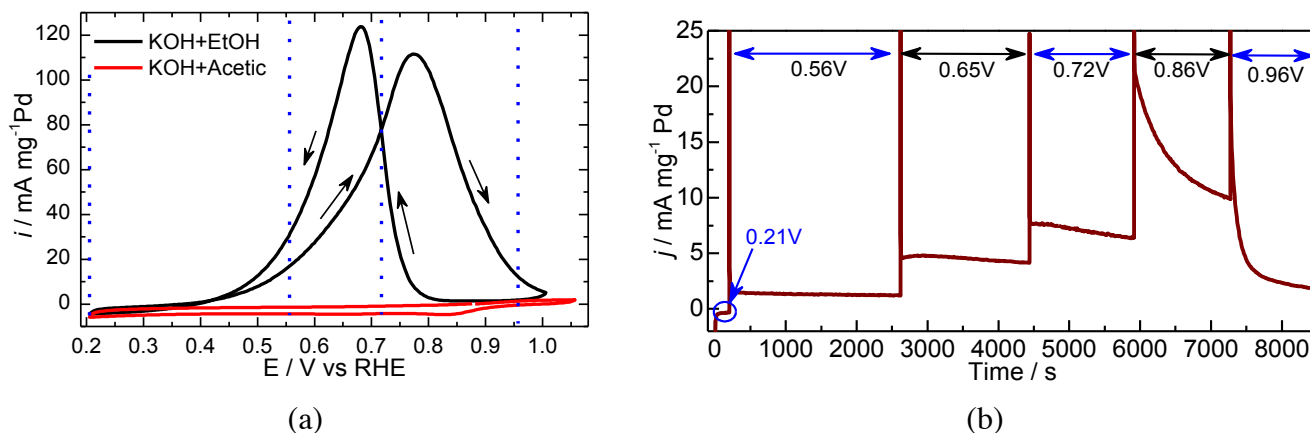


Figure 1. The CV profile for Pd/C nanoparticles in 1M (KOH + EtOH) and 1M (KOH + Acetic) at $v = 5 \text{ mV s}^{-1}$ (a), and the CA profile of Pd/C nanoparticles in 1M (KOH + EtOH) at various potentials as indicated by the double arrows (b). The vertical lines and double arrows (colored blue) shows the potentials whose PM-IRRAS spectra are discussed in the text.

This ethanol electrooxidation profile (Figure 1b) is typical for alcohols and is generally interpreted as a signature of species blocking the electrocatalyst surface at higher potential that can be removed while scanning back to lower potentials hence allowing oxidation of fresh ethanol molecules.^{19,64,65} To gain insights of the processes taking place at different potentials of the CV profile, chronoamperometry coupled with PM-IRRAS were used and the resulting data is discussed in the following section.

3.2 Identification of ethanol electrooxidation products on Pd/C surface and in the bulk electrolyte solution

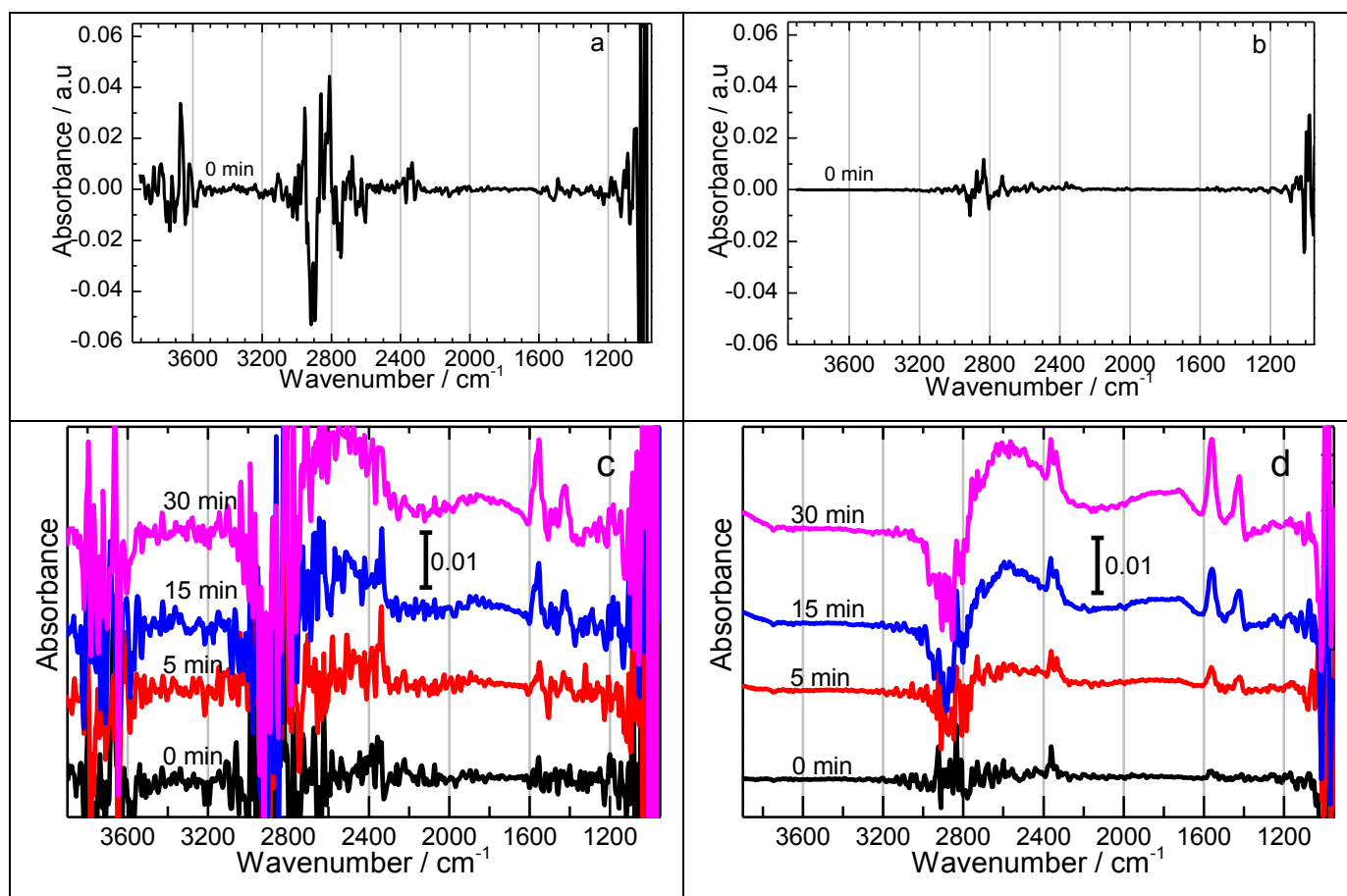
Chronoamperometry measurements were coupled with *in-situ* polarization-modulation infrared reflection absorption spectroscopy (PM-IRRAS) to identify ethanol electrooxidation products at different potentials. Figure 1b shows the resulting current/potential CA response, in which the potential was stepped up from 0.21 V/RHE to 0.96 V/RHE while collecting spectra at each potential in

increments of 5 minutes up to 30 minutes. The spectra collected at 0.21, 0.56, 0.72, and 0.96 V/RH are shown in Figure 2(a)-(h). As presented above and in the SI, the PM-IRRAS unlike the regular IRRAS technique allows us to distinguish between the oxidation species on/near the electrode surface (using the difference absorption intensities of p- and s-polarized reflection) and the oxidation species in the bulk/liquid-phase electrolyte within the thin-cavity between the CaF₂ window and the electrode (using the average absorption intensities of p- and s-polarized reflection). Herein, the spectra for the species on the electrode surface and spectra of the sum species in the thin-cavity will be referred to as “surface” and “bulk solution” species, respectively.⁶⁶

Prior to the measurement of ethanol electrooxidation species spectra, it is important to ensure that there is no atmospheric CO₂ and water vapor in the optical path which would not only decrease the IR intensity but also would contribute to observed spectra features. Especially the presence of CO₂ is critical because it is one of the anticipated ethanol oxidation products. This objective was accomplished by purging the electrolyte and the cell chamber (PMA 50) with nitrogen gas and the level of CO₂ in the system was tracked by collecting a series of background PM-IRRAS spectra at open circuit potential i.e. no applied potential. Figure S7 shows the background surface and bulk species spectra collected at various time intervals. The first spectrum (Figure S7 curve(s) (a)) was collected at the beginning of the experiment i.e. 2.5 hours before actual measurements were started. Two other spectra were collected at 30 minutes Figure S7 curve (b) and at 3 minutes Figure S7 curve (c) before the actual measurements were done. In summary, it was determined that after 2.5 hours there was no significant background contribution to interfere with any spectra features as confirmed by the straight line of Figure S7 curve(s) c). Now we shift our attention to the spectra features obtained at the various potentials as shown in Figure 2. The potentials reported were selected from the different regions of the CV profile (Figure 1a)

and are meant to shed more insights of the reaction dynamics and/or intermediates/products at those regions.

Figure 2 (a & b) shows the PM-IRRAS spectra at 0.21 V/RHE where there is no ethanol electrooxidation according to CV and CA (Figure 1). At this potential we see a negative peak centered around 2908 cm^{-1} which is due to breaking of the C – H bond. There are also two positive peaks centered on 2819 cm^{-1} and 3668 cm^{-1} which corresponds to C – H and H_2O vibrations, respectively. These observations tell us that there is some form of re-organization of the electrolyte molecules on the electrode surface. On the other hand, we do not see any significant structural changes features in bulk solution as shown by the straight line in Figure 2b. This is expected at this low potential.



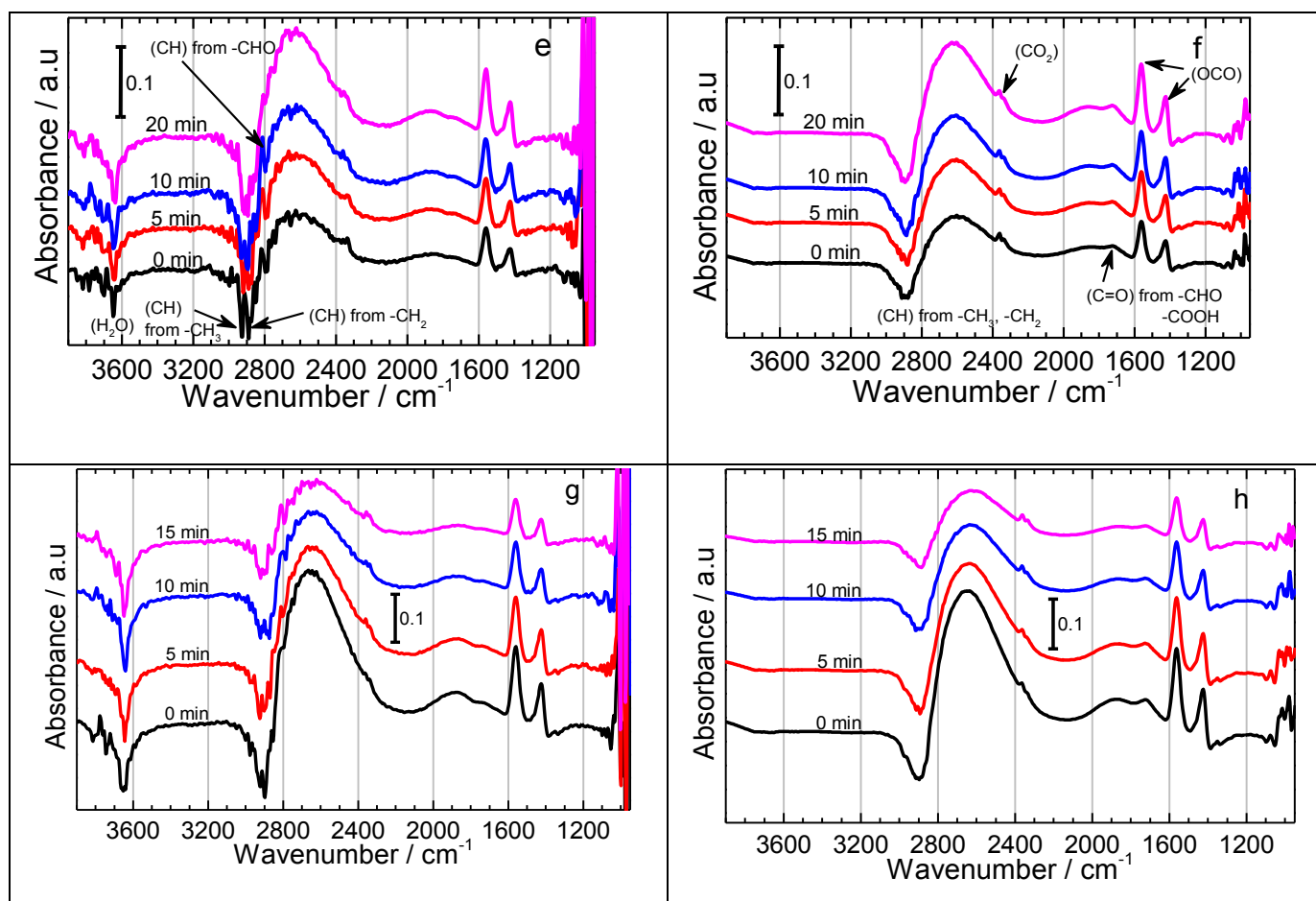


Figure 2. PM-IRRAS spectra for ethanol electrooxidation products on Pd/C nanoparticles in 1M (KOH + C₂H₅OH) at 0.21 V (a, b), 0.56 V (c, d), 0.72 (e, f), and 0.96 V (g, h) vs RHE. The left panels show oxidation species on the surface and the right panels show oxidation species in the thin-cavity/bulk solution. The spectra were processed using equation 3 and the reference spectrum was collected at the open circuit potential, see SI for details. At each potential (row), the y-scale was made the same for easy/direct comparison between surface and bulk species.

Figure 2 (c & d) shows the surface and bulk solution species at 0.56 V/RHE, which is closer to the onset potential for ethanol electrooxidation. The surface species spectra look very noisy compared with the bulk solution spectra. This phenomenon can be attributed to the dynamic activities taking place on the electrode surface at this potential. Of top interest at this potential, is the evidence of the C – C bond cleavage to form CO₂ due to the positive peak at 2353 cm⁻¹. With the PM-IRRAS we were even able to distinguish that the produced CO₂ quickly desorbs/diffuses into the bulk solution as shown by the

intensity of the peak. The conversion of CO₂ into carbonate was not evident (see Figure S2) in this work probably due to the changing pH conditions within the thin-cavity from alkaline to neutral/acidic.⁶⁷ One can notice that while the amount of CO₂ increases clearly with time at lower potential (0.56V), its accumulation is hampered or overshadowed by other species at higher potential. Although, the formation of CO during EOR on Pd in alkaline has been reported,²¹ we do not have evidence to support that argument in our spectra even after SNIFTIR treatment of our data as claimed in ref 21. Our data collaborates well with other similar work in literature where CO was not observed.¹² Therefore, the formation of CO during C – C bond cleavage maybe regarded to be a very fast process as it is directly converted to observed CO₂ at the lower potentials.

The presence of positive peaks at 1560 cm⁻¹(strong), 1423 cm⁻¹ (medium), and 1350 cm⁻¹(weak) on the surface and bulk solution spectra in **Figure 2** (c) – (h), corresponds to the asymmetric, symmetric, and C-H bending vibrations from the acetate (CH₃COO⁻) produced during ethanol electrooxidation in agreement with other literature reports.^{19,21,68} These peak assignments were confirmed with transmission infrared spectroscopy as shown in Figure S2 and the use DFT simulations as reported in **Table 1**. The simulated spectra in solution (continuum model) show the same three peaks (1558 cm⁻¹; 1410 cm⁻¹; 1334 cm⁻¹). The strongest peak is also the one at 1558 cm⁻¹ and corresponds to the asymmetric COO⁻ vibrations. The corresponding symmetric mode vibrates at 1334 cm⁻¹ and has the second highest intensity. Finally, the peak around 1410 cm⁻¹ corresponds to bending modes of the CH₃ group and features only a weak intensity. The relative positioning of the weak C – H bending and strong COO⁻ symmetric stretch are inverted in the DFT computations compared to experiment. This has already been reported in the literature.⁶⁹ Depending on the functional,⁷⁰ the C-H bending and symmetric COO stretching frequencies are more or less mixed, leading to intensity redistributions between the C-H and COO modes, suggesting that anharmonicity should be accounted for. Due to the very high

computational cost of such a treatment, this is, however, beyond the scope of this paper. The COO⁻ symmetric stretch is red-shifted in our computations by about 100 cm⁻¹.

Table 1. Normal modes (in cm⁻¹) for acetate in the region 1200-1600 cm⁻¹ (i) as obtained experimentally (see Figure S3) (ii) as computed as a function of the number of water molecules that solvate the COO⁻ moiety in solution (iii) as computed for CH₃COO adsorbed on a Pd(100) slab.

Species	COO ⁻ _{Sym}	CH	CH	COO ⁻ _{Asym}	Splitting/cm ⁻¹
(i) CH ₃ COO, exp	1423		1346	1560	137
(ii) CH ₃ COO	1334	1400	1417	1558	224
(ii) CH ₃ COO, H ₂ O	1337	1403	1417	1541	204
(ii) CH ₃ COO, 2H ₂ O	1353	1402	1418	1534	181
(ii) CH ₃ COO, 3H ₂ O	1353	1398	1416	1524	171
(iii) CH ₃ COO@Pd(100)	1360	1408	1430	1477	117

The inclusion of explicit water (see **Table 1**) mainly affects the COO⁻ stretch vibrations, with the asymmetric and symmetric mode being red- and blue-shifted by 30 and 20 cm⁻¹, respectively. This improves the mode splitting from 224 to 171 cm⁻¹ compared to the experimental 137 cm⁻¹. From **Table 1**, it is noticeable that the infrared spectrum of CH₃COO adsorbed on a Pd(100), the asymmetric vibration is also red-shifted by 80 cm⁻¹ compared to the one of CH₃COO using a continuum model for the water solvent. In addition, the two other peaks are much weaker than in solution. Thus, the comparison of the DFT simulations and the PM-IRRAS spectra shows that the “surface” species signal obtained experimentally corresponds mainly to solvated species in the interfacial water zone.

There is a remarkable difference between surface species and bulk solution species in the regions 1620 – 2000 cm⁻¹, and 3648 cm⁻¹ which also highlights the utility of PM-IRRAS technique. It is evident that the species absorbing at 1726 cm⁻¹ is mainly available in the bulk solution but not on/or near the electrode surface. This peak corresponds to C=O stretching vibrations of an aldehyde/ketone or acetic acid. Our DFT simulations for acetaldehyde show a strong peak at 1720 cm⁻¹ (C=O) but also two weak peaks between 1300-1400 cm⁻¹ (C – H bending), overlapping with the weaker peaks of acetate and one

strong peak at 2812 cm^{-1} (C – H stretch), overlapping also with a broad band centered around 2600 cm^{-1} . The origin of the broad peak at 2600 cm^{-1} would be due to accumulation of combination of various intermediates (ethoxy, acetaldehyde & its hydrate form, and acetic acid) in the thin-cavity as shown in Figure S3. Figure S3a shows the simulated spectra for ethoxy ($\text{CH}_3\text{CH}_2\text{O}$), acetaldehyde (CH_3CHO), hydrated acetaldehyde (CH_3CHOOH), and acetic acid (CH_3COOH), which confirms that ethoxy and hydrated acetaldehyde have bands near 2600 cm^{-1} . Although, the simulated spectrum for acetic acid [Figure S3 (a)] does not show any peak between 2400 cm^{-1} and 2700 cm^{-1} , the experimental spectrum [Figure S3 (b)] shows that acetic acid has three overlapping peaks within the region. Therefore, the potential candidates for the broad peak at $2400 - 2700\text{ cm}^{-1}$ would be ascribed to a combination of ethoxy, geminal-diol, and acetic acid as a result of the changing pH during the electrooxidation. Further studies are underway to confirm the true origin of this broad peak centered on 2600 cm^{-1} . The absence of the peak at 1726 cm^{-1} on the surface spectra is probably due to the low concentration of acetaldehyde and/or its interaction with the electrode surface. The negative peak at 3648 cm^{-1} on the surface species spectra is the evidence for the consumed water molecules at the electrode surface. Note that at higher potential i.e. 0.96 V , where the catalyst surface is deactivated, the products accumulation decreases with time but no evidence for the formation of CO_2 . This observation proves that acetate is indeed the dead end for EOR in agreement with the acetate CV in Figure 1 (a). Therefore, the cleavage of C – C bond is only possible at lower potentials.

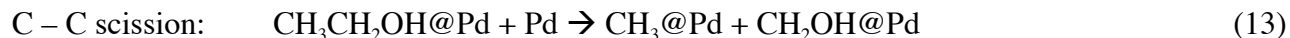
To sum up, the PM-IRRAS spectra show that at lower potential it is possible to break the C – C bond of ethanol on Pd/C in alkaline media to form CO_2 . However, the selectivity is poor due to competition towards the formation of acetate, which gets worse at higher potentials. In addition, traces of acetaldehyde are found in the bulk solution. Based on these experimental insights, we now explore the

most likely intermediates involved in the reaction path using DFT calculations as presented in the next sections.

3.3 Reaction mechanism

The reaction network involved in ethanol electro-oxidation is quite complex as presented above, even after simplifying it by considering only proton coupled electron transfers as electrochemical steps. There are 12 electrons to be recovered through 9 proton abstractions and 3 OH additions. Our simulations do not include explicitly the influence of the water-based electrolyte on the intermediates structures. However, the main determining factor is the role of OH⁻ as a proton acceptor on the thermochemistry, and this is included in the computational hydrogen electrode approach.

Furthermore, the reaction only proceeds to completion if the C – C bond can be broken. Hence, we need at least to consider the following elementary reaction steps, with specific examples given for illustration in equations (10) – (13):



To break up the complexity into smaller manageable parts, we proceed as follows: PM-IRRAS data demonstrates that the electrooxidation of ethanol over Pd leads to identifiable acetate and traces of CO₂. Therefore, for simplicity, we start by studying the intermediates that lead to acetate on the dominant Pd(111) and the more reactive and still sufficiently abundant Pd(100) surface. A brief description of the geometric features can be found in SI, we discuss here their relative energies and the most likely reaction pathway until acetate. Then, in order to obtain a "complete" picture, we have searched the most stable C₁ and C₂ intermediates at each oxidation state until CO₂. Based on this overview, we shed more

light on the reason why the reaction stops at the acetate level and why the selective cleavage of the C – C bond is difficult.

3.3.1 From ethanol to acetate

Pd(111): Figure S8 shows the adsorption structures of the most important intermediates involved in ethanol electrooxidation on Pd(111). The structures are in line with the literature⁷¹ and thus we focus here on the relative energies of the intermediates at a given oxidation state and their involvement in the oxidation path towards acetic acid. Figure 3 (a) shows the reaction energy profile for ethanol oxidation on Pd(111) at a potential of 0.26 V, based on the computational hydrogen electrode⁷ (see Computational Details). This potential corresponds to the thermodynamic equilibrium potential for the oxidation of ethanol to CO₂. In reality, over-potentials are necessarily observed but with only 0.4 V, Pd is rather promising in terms of onset potentials. Each column in the reaction coordinate corresponds to intermediates at a given oxidation state. Intermediates below and above the dotted line are due to exothermic and endothermic processes, respectively.

The ethoxy (CH₃CH₂O) species is higher in energy than the α -dehydrogenated intermediate CH₃CHOH in agreement with previous reports.⁷¹ However, Hibbits and Neurok³⁰ have modelled the oxidation of EtOH by O₂ in which the catalyst surface was pre-covered with O and OH species and have shown that the formation of ethoxy has the lowest activation barrier in these conditions, proving that it is an important intermediate. The CH₂CH₂OH is intermediate in energy. A second proton coupled electron transfer leads to an oxidation state which is particularly challenging to describe realistically: three adsorbed intermediates are connected through well-known solution equilibria: acetaldehyde, its hydrate (the geminal diol) and the enol; the fourth intermediate considered (CH₃COH) is strongly bound to the metal surface and can only indirectly participate in the equilibrium.

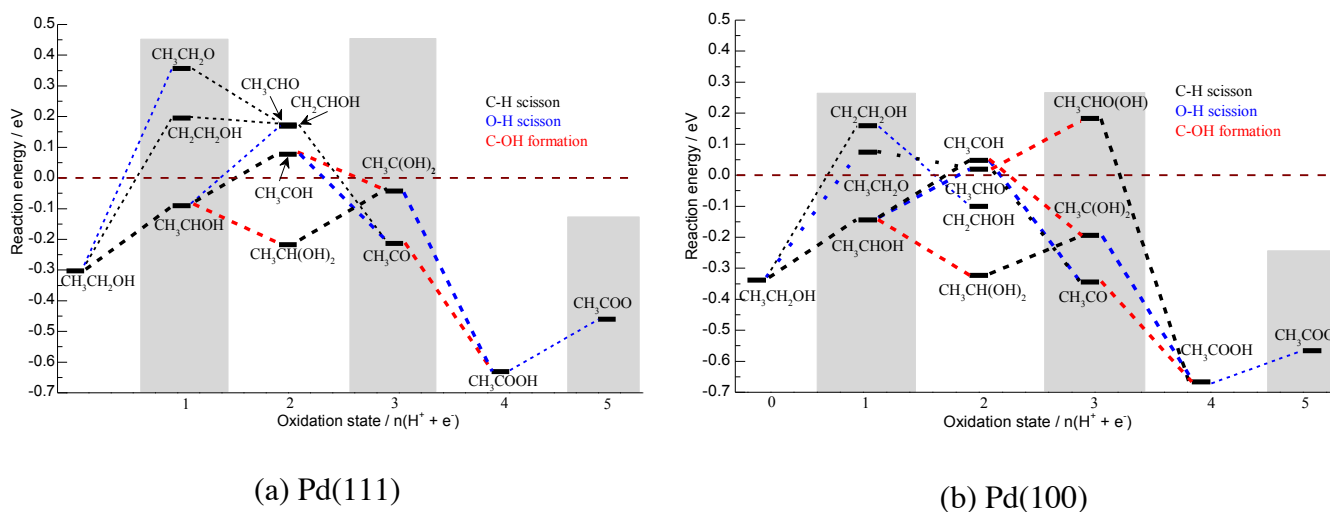


Figure 3. Reaction energy profile for ethanol oxidation on (a) Pd(111) surface and (b) Pd(100) surface at a potential of 0.26 V vs RHE. Only the most important (and low lying) intermediates are shown. The dotted line connecting the intermediates are color coded according to the reaction process taking place, black and blue correspond to C – H and O – H bond scission, respectively while red corresponds to C – O bond formation

On the surface, acetaldehyde and its enol are almost iso-energetic. Since the CH_2C_x intermediates at the following oxidation states are significantly higher in energy than the CH_3C_x intermediates, we consider the enol to be a dead end, i.e., it just participates in the equilibria if formed. In fact, it is rather the hydrate which is the dominant intermediate: it is the lowest energy intermediate, is connected to the previous lowest energy intermediate and can form either in solution through acetaldehyde or on the surface by a surface OH assisted process.

The oxidation of the hydrate does not lead to the lowest energy intermediate at oxidation state +3. The lowest energy intermediate at oxidation state +3 is the acetyl (CH_3CO) and it is only accessible from higher energy intermediates of the previous oxidation state +2. Oxidation of CH_3CO or $\text{CH}_3\text{C}(\text{OH})_2$ invariably yields acetic acid, through a OH addition and a dehydrogenation, respectively. Acetic acid is by far the lowest energy intermediate on the surface at oxidation state +4 (the second lowest fragment is CH_2CO at 0.86 eV higher in energy), and can desorb easily into solution. Then, in alkaline solution the

formation of CH_3COO^- is straightforward. This reaction network explains satisfactorily the observed formation of acetic acid (or acetate at high pH values). After a quick comparison of the acetic acid formation on the Pd(100) surface, the following sections investigate the prospects to split the C – C bond in ethanol.

Pd(100): Figure S9 shows the adsorption structures of the most important intermediates involved in ethanol electrooxidation on Pd(100). The geometry of the adsorbates is very similar to that on Pd(111) and is therefore not discussed any further.

Figure 3 (b) shows the reaction energy profile for ethanol electrooxidation on Pd(100) surface at a potential of 0.26 V. Here we highlight the differences between Pd(100) surface and Pd(111). One difference is that the reaction energies are shifted to lower energies by ca. 0.1 – 0.2 eV, meaning that the (100) surface is more reactive than the (111) surface in agreement with previous reports.^{72,73,74} The second difference is that the relative stability of acetaldehyde (CH_3CHO) and 1-hydroxyethylidene (CH_3COH) is reversed: on the 100 surface, CH_3CHO is 0.02 eV more stable than CH_3COH . However, it is doubtful that these very small energy differences are representative of the situation under electro-catalytic conditions where the solvent and the potential may easily change the relative energies by more than this difference. In any case, the geminal-diol is the lowest intermediate at this oxidation state for both surfaces. Therefore, we can conclude that investigating the Pd(100) or Pd(111) surface is qualitatively the same. Nevertheless, since the (100) surface is more active for bond formation and splitting reactions,⁷⁴ and these reactions are key and highly activated on this surface (*vide infra*), we report only the results for Pd(100) in the remainder of this article. Based on our DFT results, we can also predict the overpotential to produce CH_3COOH from EtOH on Pd catalysts and this overpotential is in agreement with the onset potential observed experimentally. The lowest energy path is represented at various potentials in **Figure 4**. It starts with the generation of CH_3CHOH , an endothermic step at 0.26 V.

It yields the gem-diol $\text{CH}_3\text{CH}(\text{OH})_2$ at the degree of oxidation +3 that is further dehydrogenated into $\text{CH}_3\text{C}(\text{OH})_2$, a step that is also endothermic at this potential. The last step is strongly exothermic and gives CH_3COOH . At 0.45 V, all the steps along the most stable path to CH_3COO^- are predicted being endothermic. At that potential, even the generation of acetaldehyde starts to be exothermic. Those potentials are in line with our experimental results (CV in Figure 1 and the PM-IRRAS spectra in Figure 2) where the reaction starts at around 0.45 V and where traces of acetaldehyde are identified at 0.65 V/RHE and more intense at 0.72 V.

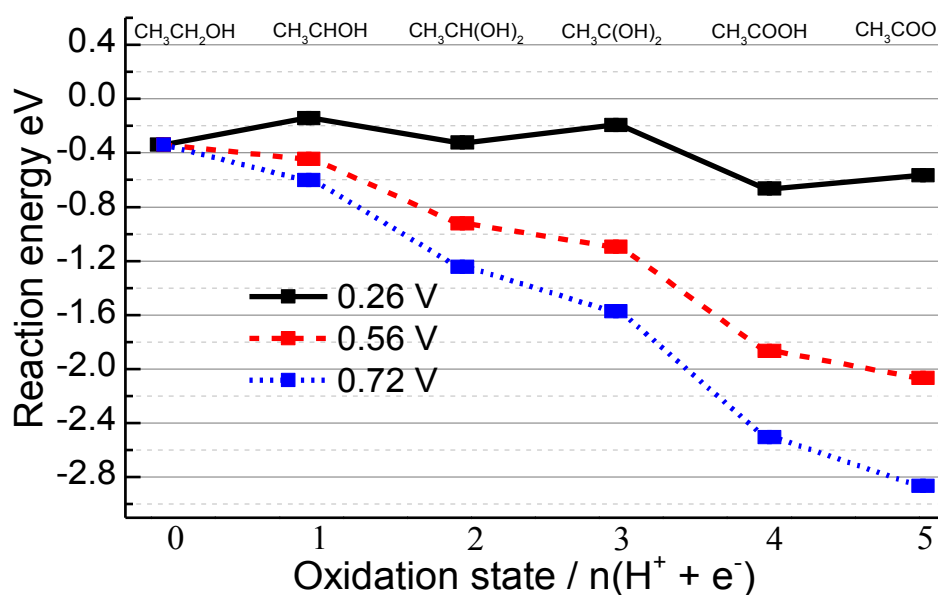


Figure 4. Reaction energy profiles for ethanol electrooxidation on Pd(100) surface showing the effect of the electrochemical potential (0.26 V, 0.56 V, and 0.72 V vs RHE) for the most likely C2 reaction path.

3.3.2 Intermediates beyond Acetate and Breaking the C - C bond

The chemical viability of DEFCs relies on two related aspects. First, the fuel needs to be completely oxidized in order to obtain a realistically useful energy and current density. In other words, catalysts oxidizing ethanol to acetate (acetic acid in acidic media) are not useful in practice, as they would liberate only 4 out of 12 possible electrons. Second, the kinetics needs to be efficient at a reasonably low over-potential. According to the Butler-Volmer equation, a proton coupled electron transfer is directly

accelerated by the over-potential. Furthermore, the barriers for formal dehydrogenation reactions are fairly small on Pd (in the order of 0.7 eV). While the C–OH formation could be somewhat more activated, it can equally be considered an electrochemical step and therefore its barrier is likely to be heavily lowered by the over-potential and the presence of surface hydroxyls. If the C–C dissociation were coupled with the formation of the C–OH bond, in a concerted mechanism with the hydroxide anion attacking from the solvent, this dissociation would also strongly depend on the electrochemical potential. However, modeling such a process would require a full description of the solvent and a complete inclusion of the electrochemical potential, which is out of the scope of this study. The direct C–C bond splitting, in contrast, is a chemical step and thus hardly affected by the electrochemical potential as extrapolated from our findings for the electro-carboxylation of ethene.⁷⁵ Hence, investigating the feasibility of C – C bond splitting is key in order to understand both, incomplete oxidation and sluggish kinetics and this can be done without the inclusion of the electrochemical potential.

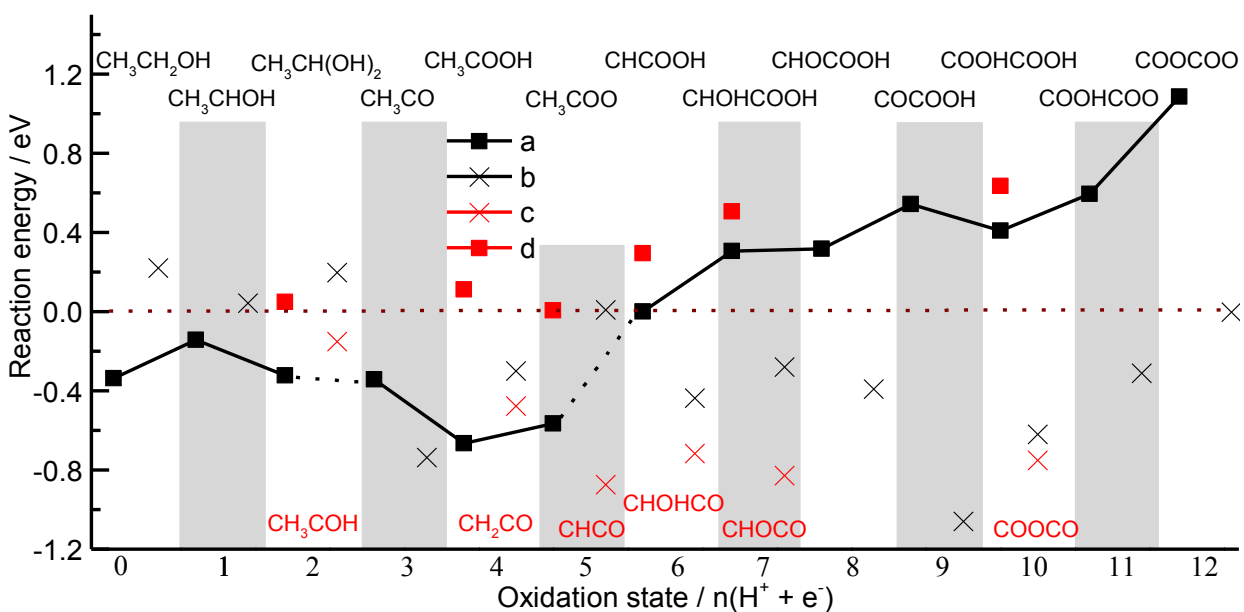


Figure 5. Global reaction energy profile of the most stable intermediates during ethanol electrooxidation process on Pd(100) at 0.26 V/RHE. The black squares show the most stable C₂ intermediates at each oxidation state (C₂ path) whose intermediates are indicated at the top. To guide the eyes, a line has been added, in solid (resp. dotted) when the intermediates are connected (resp. not) from one oxidation state to the next. Legend: (a) Most stable C₂ species, (b) C₁ fragments generated from the most stable C₂, (c) Most stable C₁ fragments, and (d) Parent C₂ species of the most stable C₁ fragments which are shown at the bottom.

Let us start by addressing the first question: which is the most likely possible path that would lead from ethanol to CO₂ instead of acetic acid based on thermodynamics? Figure 5 summarizes our effort to identify the lowest energy intermediates at each of the 12 oxidation states, accounting for C – H, O – H and C – C bond activations as well as C – OH bond formation. The intermediates below the zero horizontal dashed line in **Figure 5** are due to an exothermic process while those above the line are due to an endothermic process at the potential of 0.26 V i.e. the minimum potential for which ethanol oxidation is energetically feasible in terms of free energy. At each oxidation state we indicate the most stable C₂ intermediate and the energy of its C – C bond broken C₁ analogue. Of course, at any given oxidation step, the lowest intermediate before the C – C bond breaking does not need to yield the lowest two C₁ fragments at that oxidation step, which is indicated by the presence of open circles on **Figure 5**. Note that we did not consider additional "pure" chemical steps which further complicate the reaction network, e.g. by introducing formic acid (HCOOH) at the same oxidation state as CO. Similarly, the lowest energy intermediate at each oxidation state “n” is not necessarily directly related to the intermediate of oxidation state “n+1” (e.g., CH₃CH₂(OH)₂ is the most stable intermediate at oxidation state +2, but at +3, it is CH₃CO), which is indicated by broken black lines instead of the full lines.

As mentioned in the introduction, ethanol electrooxidation mechanism is best presented in a “dual path mechanism scheme”. The C₂ path does not involve the breaking of the C – C bond while in the C₁ the C – C bond yielding C₁ fragments. In agreement with previous reports,³¹ we found a reasonably well-connected C₂ pathway up to CH₃COO (+5). However, from +5 to +6, the lowest energy intermediate

changes dramatically from CH_3COO to CHCOOH . Furthermore, the process is endothermic by 0.6 eV at the thermodynamic equilibrium potential for the overall reaction. This implies that a potential of at least 0.6 V would be necessary to drive the oxidation beyond acetate (acetic acid). The fact that these intermediates are not connected would mean a further increase of the over-potential. This is in agreement with the cyclic voltammetry experiments demonstrating that acetic acid is inert for further oxidation, i.e. no current transfer was observed in the CVs with 1M ($\text{KOH}+\text{CH}_3\text{COOH}$) solution as shown in Figure 1. To conclude, **Figure 5** indicates that it would be ideal to split the C – C bond before reaching acetate (acetic acid in acid media), which is the dead end of the reaction with the current catalysts. On the other hand, on thermodynamic grounds, the C – C bond splitting is "constantly" beneficial from oxidation state +6 onwards and, in general, passing to the C_1 pathway is more likely when the C_2 fragment can be split through a de-carbonylation, generating a highly stable CO moiety.

Turning to the second limitation, i.e., the sluggish kinetics, we investigate the reasons for which the C – C bond is not split before reaching acetic acid. Both for ethanol and for the first oxidative intermediate, the C – C bond breaking is highly unlikely as the thermodynamics are fairly unfavorable. However, at oxidation state +2 and +3 the breaking of the C–C bond could occur based on thermodynamic grounds. So why is it barely observed experimentally? To answer this question, we have identified transition states for breaking the C – C bond in the key intermediates at oxidation state +2 (**Figure 6a**) and +3 (**Figure 6b**).

The first, general observation is that the activation energies are quite high with about 1.3 eV, even on the Pd(100) surface which is more active than the Pd(111) surface. There are two barriers that differ significantly from this number. First, is the highest activation barrier for breaking the C – C of the hydrate, $\text{CH}_3\text{CH}(\text{OH})_2$ (oxidation state +2) ($E^\ddagger = 2.1$ eV). This large barrier is probably due to the fact that the carbons of the reactant are not interacting with the catalyst surface, hence they are not activated.

Besides, the steric crowding which destabilizes both the transition state and the product, barely affects the reactant, which does not adsorb through a carbon atom but rather through the two lone-pair of electrons of the oxygen atoms. In support of this argument, we find that the energy barrier for the dehydrogenated geminal diol is significantly lower (1.4 eV).

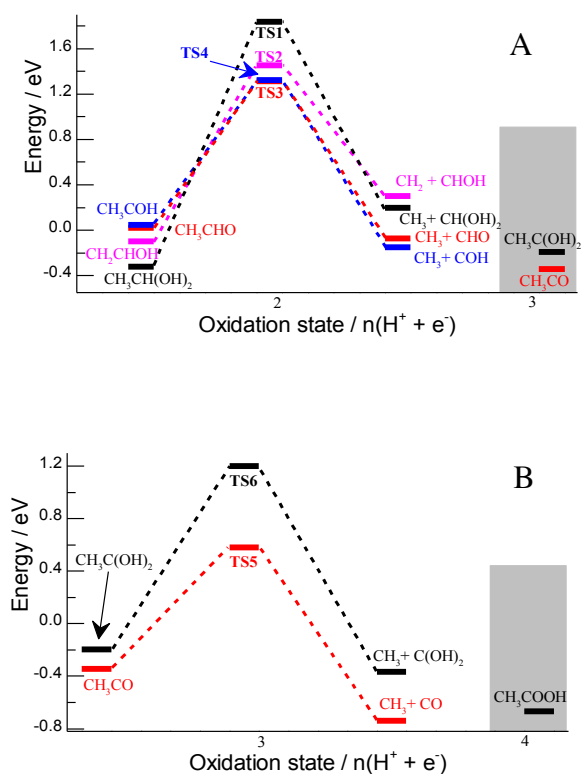


Figure 6: Energy profile for breaking the C-C bond on Pd(100) for species at oxidation state two (A) and at oxidation state three (B), both at 0.26 V vs RHE.

In this case, the steric crowding in the reactant and product is similar, as both adsorb through the unsaturated carbon atom hence benefiting from less destabilization. Second, the lowest barrier for breaking C – C bond is found for acetyl (CH_3CO) with activation energy of "only" 0.9 eV, which is attributed to the very stable CO product on Pd surface. Note, however, that this is still a significant

barrier at room temperature that cannot be lowered by the application of potential. Furthermore, the C – C splitting is in competition with the thermodynamically favorable C – OH bond formation that yields acetic acid. Playing on the structure of the catalyst, one may favor the C – C bond splitting since this is a structure-sensitive reaction that is favored on low-coordinated facets: the C – C bond splitting in CH_3CO drops from 1.4 eV on Pd(111)⁷⁶ to 0.9 eV on Pd(100) and 0.7 eV on Pd(110)⁷⁷

The reaction selectivity towards acetic acid is better understood from the aforementioned reaction energy profiles, keeping in mind the C – H and O – H bond breaking in ethanol catalyzed by Pd have a barrier lower than 0.8 eV.⁷⁸ These steps can be even further activated by the presence of surface hydroxyls as shown in previous DFT studies.^{30,31} The thermodynamic impact of the recombination of H^+ and OH^- is, however, also included in our present study through the use of the computational hydrogen electrode. At oxidation state +2 the most stable intermediate (the gem-diol $\text{CH}_3\text{CH}(\text{OH})_2$) does not undergo C – C splitting ($E^\ddagger = 2.1$ eV) and also higher lying intermediates only react slowly towards C_1 products and face a strong competition with C – OH bond formation. Hence, the hydrate gets oxidized, despite the fact that this does not lead to the lowest energy intermediate at oxidation state +3. At oxidation state +3, there are three processes in competition. In one process, the $\text{CH}_3\text{C}(\text{OH})_2$ is quickly oxidized to acetic acid ($E^\ddagger < 0.8$ eV) and the C – C bond remains intact. In the second process, the most stable but kinetically less accessible intermediate CH_3CO , can undergo slow C – C bond splitting ($E^\ddagger = 0.9$ eV) and the fragments eventually be oxidized to CO/CO_2 . In the third process, CH_3CO can be oxidized to acetic acid as explained above, which is an electrochemical process that is favored by oxidative potentials. In other words, the necessary potentials and the unfavorable "connection" between the most stable intermediates lead to the dominance of acetic acid as a product and to the small probability of splitting the C – C bond at an early stage of the oxidation process. These results show how challenging and complex it is to design a catalyst for complete electrooxidation of ethanol to CO_2 .

easily yields acetic acid. In the second route, acetaldehyde is dehydrogenated into acetyl, CH_3CO . Since acetaldehyde is less stable on the surface than its gem-diol, this route is disfavored. However, the acetyl is a pivotal intermediate. Its degree of oxidation is the first along the path where the key C – C bond scission can occur exothermically from the most stable C_2 fragment. Moreover among all the intermediates of degree +2 and +3, it is the one that exhibits the lowest activation barrier for the C – C bond scission (0.9 eV). Hence, even though a chemical step, CH_3CO decarbonylation could compete with the C – H, O – H and C – OH rearrangements that are facilitated by the electrochemical potential. Thus, the CO_2 traces we have observed experimentally at low potentials by PM-IRRAS are probably generated from adsorbed acetyl. This is in line with the ATR-SEIRAS experiments of Yang et al.¹⁹ However, the acetyl can also easily lead to acetic acid by the formation of a C – OH bond, a process that is accelerated by oxidative potentials. This explains the experimental observation that the selectivity towards CO_2 decreases at higher potential.

In summary, the C – C bond scission that is essential to open the route to a full oxidation of ethanol can occur at the degree of oxidation +3. However, it is a slow process and in competition with the faster oxidation to acetic acid. For degree of oxidation $> +5$, the C – C bond splitting is exothermic, opening the road to the C_1 pathway. However, there is a strong disconnection on the C_2 pathway between the most stable species at degree +5 (CH_3COO) and the most stable species at degree +6 (CHCOOH) that hinders the oxidation of acetate (Figure 5), in line with the experimentally observed impossibility to oxidize acetic acid in KOH under our conditions (Figure 1).

4 Conclusion

We have presented a comprehensive study of the reaction mechanism of ethanol electrooxidation over Pd surfaces, combining cyclic voltammetry (CV), polarization modulation infrared reflection absorption

spectroscopy (PM-IRRAS), and density functional theory (DFT) calculations. The PM-IRRAS information (identification of surface and bulk solution species) simplified the number of possible intermediates considered in the DFT modelling, while DFT insights provided invaluable information of the elementary reaction intermediates and kinetic parameters, which was not accessible experimentally. This strategy can be easily extended to other alcohols or organic molecules on other metal surfaces.

In this work, we have solved two of the long debated puzzles: the path leading to the formation of acetate, the product obtained over a Pd catalyst in alkaline conditions, and the most likely intermediates where the C–C bond can be broken. For the formation of acetic acid, we have identified two converging paths: the most stable path, going through the gem-diol (hydrate of acetaldehyde), and the second most stable path going through the acetyl (CH_3CO). Unfortunately, acetate cannot be oxidized further over Pd according to our CV and DFT results, closing the door to the C1 path and thus the complete oxidation of ethanol. Hence, to contribute to the second debate, we have determined the most likely intermediates where the C – C bond can be broken before reaching acetate. We have demonstrated that acetyl (at oxidation state three) has by far (>0.3 eV) the lowest activation energy for the C – C bond breaking ($E^\ddagger = 0.9$ eV). However, the over-potentials required for reasonable current densities are strongly accelerating the electrochemical oxidation process. This favors the C-OH formation over the C – C splitting reaction. Therefore, CH_3CO is quickly oxidized to acetic acid, thereby suppressing the C – C bond breaking, explaining the negligible amount of CO_2 detected at higher potentials. In other words, CH_3CO plays a pivotal role since it can either undergo a C – C bond splitting, eventually yielding CO_2 , or be oxidized towards CH_3COOH , a dead end in the reaction scheme. Through this analysis, our work has determined the conditions for a better selectivity towards CO_2 : destabilize the gem-diol, stabilize the acetyl and facilitate its splitting into CH_3 and CO. A large descriptor-based search of catalysts is being started to find *in silico* alloy formulations that would obey to these conditions.

Acknowledgement

The authors thank University of Ottawa, CNRS and ENS Lyon for support in the frame of the associated international laboratory FUNCAT "Fundamental catalysis for green chemistry: From well-defined active sites to mechanistic explorations", Natural Sciences and Engineering Research Council of Canada (NSERC) for financial support, Canada Foundation for Innovation (CFI) for equipment funding and the PSMN and Compute Canada (Sharcnet) for the computational resources.

Supporting Information Available: The physical characterization of the Pd/C nanoparticles; the PM-IRRAS background/reference and Data processing and interpretation details; FTIR transmission spectra for KOH and (KOH+ acetic acid, sodium acetate, sodium carbonate, and ethanol); most stable geometric ethanol oxidation intermediates structures and some of the key POSCAR files. This material is available free of charge via the Internet at <http://pubs.acs.org>

References

- (1) Heinzl, A.; Cappadonia, M.; Stimming, U.; Kordesch, K. V.; Tambasco de Oliveira, J. C. In *Ullmann's Encyclopedia of Industrial Chemistry*; Wiley-VCH, 2010.
- (2) Jiang, S. P.; Wang, X. In *Solid State Electrochem. II*; Wiley-VCH Verlag GmbH & Co. KGaA, 2011; pp. 179–264.
- (3) Steele, B. C. H.; Heinzl, A. *Nature* **2001**, *414*, 345–352.
- (4) Zhang, S.; Shao, Y.; Yin, G.; Lin, Y. *J. Mater. Chem.* **2013**, *1*, 4631–4641.
- (5) An, L.; Zhao, T. S.; Li, Y. S. *Renew. Sustain. Energy Rev.* **2015**, *50*, 1462–1468.
- (6) Goldemberg, J. *Science* **2007**, *315*, 808–810.
- (7) Nørskov, J. K.; Rossmeisl, J.; Logadottir, A.; Lindqvist, L.; Kitchin, J. R.; Bligaard, T.; Jónsson, H. *J. Phys. Chem. B* **2004**, *108*, 17886–17892.
- (8) Varcoe, J. R.; Atanassov, P.; Dekel, D. R.; Herring, A. M.; Hickner, M. A.; Kohl, P. A.; Kucernak, A. R.; Mustain, W. E.; Nijmeijer, K.; Scott, K.; Xu, T.; Zhuang, L.; Zhuang; Zhuang; Zhuang; Zhuang; *Energy & Environ. Sci.* **2014**, *7*, 3135–3191.
- (9) Fujiwara, N.; Siroma, Z.; Yamazaki, S.; Ioroi, T.; Senoh, H.; Yasuda, K. *J. Power Sources* **2008**, *185*, 621–626.
- (10) Ma, L.; Chu, D.; Chen, R. *Int. J. Hydrog. Energy* **2012**, *37*, 11185–11194.
- (11) Bianchini, C.; Shen, P. K. *Chem. Rev.* **2009**, *109*, 4183–4206.
- (12) Fang, X.; Wang, L.; Shen, P. K.; Cui, G.; Bianchini, C. *J. Power Sources* **2010**, *195*, 1375–1378.
- (13) Xu, C.; Shen, P. kang; Liu, Y. *J. Power Sources* **2007**, *164*, 527–531.
- (14) Martinez, U.; Serov, A.; Padilla, M.; Atanassov, P. *ChemSusChem* **2014**, *7*, 2351–2357.

- (15) M. Koper, M. T.; S. Lai, S. C. *Faraday Discuss.* **2009**, *140*, 399–416.
- (16) Tremiliosi-Filho, G.; Gonzalez, E. R.; Motheo, A. J.; Belgsir, E. M.; Leger, J.-M.; Lamy, C. J. *Electroanal. Chem.* **1998**, *444*, 31–39.
- (17) Tarasevich, M. R.; Korchagin, O. V. *Russ. J. Electrochem.* **2013**, *49*, 600–618.
- (18) Geraldes, A. N.; Furtunato da Silva, D.; Martins da Silva, J. C.; Antonio de Sá, O.; Spinacé, E. V.; Neto, A. O.; Coelho dos Santos, M. J. *Power Sources* **2015**, *275*, 189–199.
- (19) Yang, Y.-Y.; Ren, J.; Li, Q.-X.; Zhou, Z.-Y.; Sun, S.-G.; Cai, W.-B. *ACS Catal.* **2014**, *4*, 798–803.
- (20) Zhou, Z.-Y.; Sun, S.-G. *Electrochim. Acta* **2005**, *50*, 5163–5171.
- (21) Zhou, Z.-Y.; Wang, Q.; Lin, J.-L.; Tian, N.; Sun, S.-G. *Electrochimica Acta* **2010**, *55*, 7995–7999.
- (22) Christensen, P. A.; Jones, S. W. M.; Hamnett, A. J. *Phys. Chem. C* **2012**, *116*, 24681–24689.
- (23) Christensen, P. A.; Linares-Moya, D. J. *Phys. Chem. C* **2010**, *114*, 1094–1101.
- (24) Christensen, P. A.; Hamnett, A.; Linares-Moya, D. *Phys. Chem. Chem. Phys.* **2011**, *13*, 11739–11747.
- (25) Christensen, P. A.; Jones, S. W. M. *J. Phys. Chem. C* **2014**, *118*, 29760–29769.
- (26) Cantane, D. A.; Lima, F. H. B. *Electrocatalysis* **2012**, *3*, 324–333.
- (27) Liu, J.; Ye, J.; Xu, C.; Jiang, S. P.; Tong, Y. *Electrochem. Commun.* **2007**, *9*, 2334–2339.
- (28) Liang, Z. X.; Zhao, T. S.; Xu, J. B.; Zhu, L. D. *Electrochimica Acta* **2009**, *54*, 2203–2208.
- (29) Schnur, S.; Groß, A. *Catal. Today* **2011**, *165*, 129–137.
- (30) Hibbitts, D. D.; Neurock, M. J. *Catal.* **2013**, *299*, 261–271.
- (31) Sheng, T.; Lin, W.-F.; Hardacre, C.; Hu, P. J. *Phys. Chem. C* **2014**, *118*, 5762–5772.
- (32) Delpeuch, A. B.; Chatenet, M.; Rau, M. S.; Cremers, C. *Phys. Chem. Chem. Phys.* **2015**, *17*, 10881–10893.
- (33) Ferrin, P.; Mavrikakis, M. *J. Am. Chem. Soc.* **2009**, *131*, 14381–14389.
- (34) Ferrin, P.; Nilekar, A. U.; Greeley, J.; Mavrikakis, M.; Rossmeisl, J. *Surf. Sci.* **2008**, *602*, 3424–3431.
- (35) Rossmeisl, J.; Ferrin, P.; Tritsarlis, G. A.; Nilekar, A. U.; Koh, S.; Bae, S. E.; Brankovic, S. R.; Strasser, P.; Mavrikakis, M. *Energy & Environ. Sci.* **2012**, *5*, 8335–8342.
- (36) Anderson, A. B.; Albu, T. V. *J. Am. Chem. Soc.* **1999**, *121*, 11855–11863.
- (37) Lozovoi, A. Y.; Alavi, A. *Phys. Rev. B: Condens. Matter Mater. Phys.* **2003**, *68*, 245416/1–245416/18.
- (38) Otani, M.; Sugino, O. *Phys. Rev. B: Condens. Matter Mater. Phys.* **2006**, *73*, 115407/1–115407/11.
- (39) Taylor, C.; Wasileski, S.; Filhol, J.-S.; Neurock, M. *Phys. Rev. B* **2006**, *73*.
- (40) Fang, Y.-H.; Liu, Z.-P. *J. Phys. Chem. C* **2009**, *113*, 9765–9772.
- (41) Skulason, E.; Karlberg, G. S.; Rossmeisl, J.; Bligaard, T.; Greeley, J.; Jonsson, H.; Norskov, J. K. *Phys. Chem. Chem. Phys.* **2007**, *9*, 3241–3250.
- (42) Mathew, K.; Sundararaman, R.; Letchworth-Weaver, K.; Arias, T. A.; Hennig, R. G. *J. Chem. Phys.* **2014**, *140*, 084106/1–084106/8.
- (43) Jinnouchi, R.; Anderson, A. B. *Phys. Rev. B* **2008**, *77*, 245417–245435.
- (44) Filhol, J.-S.; Neurock, M. *Angew. Chem., Int. Ed.* **2006**, *45*, 402–406.
- (45) Steinmann, S. N.; Michel, C.; Schwiedernoch, R.; Filhol, J.-S.; Sautet, P. *ChemPhysChem* **2015**, *16*, 2307–2311.
- (46) Janik, M.; Taylor, C.; Neurock, M. *Top. Catal.* **2007**, *46*, 306–319.
- (47) Fang, Y.-H.; Wei, G.-F.; Liu, Z.-P. Theoretical modeling of electrode/electrolyte interface from first-principles periodic continuum solvation method. *Catalysis Today*, 2013, *202*, 98–104.
- (48) Figlarz, M.; Fievet, F.; Lagier, J. P. Reduction of metal compounds to metal powders by polyols.,

June 22, 1984.

- (49) Monyoncho, E. A.; Ntais, S.; Soares, F.; Woo, T. K.; Baranova, E. A. *J. Power Sources* **2015**, *287*, 139–149.
- (50) Zamlynny, V.; Lipkowski, J. In *Advances in Electrochemical Science and Engineering: Diffraction and Spectroscopic Methods in Electrochemistry*; Wiley-VCH Verlag GmbH, 2006; Vol. 9, pp. 315–376.
- (51) Golden, W. G.; Dunn, D. S.; Overend, J. J. *Catal.* **1981**, *71*, 395–404.
- (52) Kresse, G.; Hafner, J. *Phys. Rev. B: Condens. Matter* **1993**, *48*, 13115–13118.
- (53) Kresse, G.; Furthmüller, J. *Phys. Rev. B: Condens. Matter* **1996**, *54*, 11169–11186.
- (54) Perdew, J. P.; Burke, K.; Ernzerhof, M. *Phys. Rev. Lett.* **1996**, *77*, 3865–3868.
- (55) Kresse, G.; Joubert, D. *Phys. Rev. B: Condens. Matter Mater. Phys.* **1999**, *59*, 1758–1775.
- (56) Blochl, P. E. *Phys. Rev. B: Condens. Matter* **1994**, *50*, 17953–17979.
- (57) Methfessel, M.; Paxton, A. T. *Phys. Rev. B* **1989**, *40*, 3616–3621.
- (58) Henkelman, G.; Jonsson, H. *J. Chem. Phys.* **2000**, *113*, 9978–9985.
- (59) Fleurat-Lessard, P.; Dayal, P. Opt'n Path <http://perso.ens-lyon.fr/paul.fleurat-lessard/ReactionPath.html> (accessed 2015).
- (60) Henkelman, G.; Jonsson, H. *J. Chem. Phys.* **1999**, *111*, 7010–7022.
- (61) Hafner, D. K. and T. B. and J. J. *Physics: Condens. Matter* **2010**, *22*, 265006.
- (62) Mennucci, B.; Cancès, E.; Tomasi, J. *J. Phys. Chem. B* **1997**, *101*, 10506–10517.
- (63) Frisch, M. J.; Fox, D. J.; Cioslowski, J.; Ortiz, J. V.; Foresman, J. B.; Farkas, O.; Daniels, A. D.; Dapprich, S.; Dannenberg, J. J.; Salvador, P.; Voth, G. A.; Zakrzewski, V. G.; Morokuma, K.; Martin, R. L.; Ochterski, J. W.; Pomelli, C.; Cammi, R.; Austin, A. J.; Yazyev, O.; Stratmann, R. E.; Gomperts, R.; Jaramillo, J.; Adamo, C.; Bakken, V.; Cross, J. B.; Knox, J. E.; Klene, M.; Millam, J. M.; Rega, N.; Cossi, M.; Tomasi, J.; Iyengar, S. S.; Burant, J. C.; Rendell, A.; Raghavachari, K.; Normand, J.; Kobayashi, R.; Staroverov, V. N.; Kudin, K. N.; Brothers, E.; Heyd, J. J.; Bearpark, M.; Ogliaro, F.; Peralta, J., J. E.; Montgomery, J. A.; Vreven, T.; Nakai, H.; Kitao, O.; Honda, Y.; Nakajima, T.; Ishida, M.; Hasegawa, J.; Fukuda, R.; Toyota, K.; Ehara, M.; Hada, M.; Sonnenberg, J. L.; Zheng, G.; Bloino, J.; Izmaylov, A. F.; Hratchian, H. P.; Li, X.; Caricato, M.; Nakatsuji, H.; Petersson, G. A.; Mennucci, B.; Barone, V.; Scalmani, G.; Cheeseman, J. R.; Robb, M. A.; Scuseria, G. E.; Schlegel, H. B.; Trucks, G. W. *Gaussian09*, 2013.
- (64) Habibi, B.; Mohammadyari, S. *Int. J. Hydrog. Energy* **2015**, *40*, 10833–10846.
- (65) Schechter, J. M.; Yang, Y.; Li, X.; Zhao, Y. *RSC Adv.* **2016**, *6*, 5384–5390.
- (66) Monyoncho, E. A.; Ntais, S.; Brazeau, N.; Wu, J.-J.; Sun, C.-L.; Baranova, E. A. *ChemElectroChem* **2016**, *3*, 218–227.
- (67) Ferreira Jr., R. S.; Janete Giz, M.; Camara, G. A. *J. Electroanal. Chem.* **2013**, *697*, 15–20.
- (68) Christensen, P. A.; Jones, S. W. M.; Hamnett, A. *Phys. Chem. Chem. Phys.* **2013**, *15*, 17268–17276.
- (69) Rudolph, W. W.; Fischer, D.; Irmer, G. *Dalton Trans.* **2014**, *43*, 3174–3185.
- (70) Sutton, C. C. R.; Franks, G. V.; da Silva, G. *Spectrochim. Acta Part A: Mol. Biomol. Spectrosc.* **2015**, *134*, 535–542.
- (71) Alcalá, R.; Mavrikakis, M.; Dumesic, J. A. *J. Catal.* **2003**, *218*, 178–190.
- (72) Wang, E. D.; Xu, J. B.; Zhao, T. S. *J. Phys. Chem. C* **2010**, *114*, 10489–10497.
- (73) Buso-Rogero, C.; Grozovski, V.; Vidal-Iglesias, F. J.; Solla-Gullon, J.; Herrero, E.; Feliu, J. M. *J. Mater. Chem.* **2013**, *1*, 7068–7076.
- (74) Li, H.; Calle-Vallejo, F.; Kolb, M. J.; Kwon, Y.; Li, Y.; Koper, M. T. M. *J. Am. Chem. Soc.* **2013**, *135*, 14329–14338.

- (75) Steinmann, S. N.; Michel, C.; Schwiedernoch, R.; Wu, M.; Sautet, P. *J. Catal.* **2016** in press.
- (76) Li, M.; Guo, W.; Jiang, R.; Zhao, L.; Shan, H. *Langmuir* **2010**, *26*, 1879–1888.
- (77) Guo, W.; Li, M.; Lu, X.; Zhu, H.; Li, Y.; Li, S.; Zhao, L. *Dalton Trans.* **2013**, *42*, 2309–2318.
- (78) Zaffran, J.; Michel, C.; Delbecq, F.; Sautet, P. *J. Phys. Chem. C* **2015**, *119*, 12988–12998.
- (79) Michel, C.; Zaffran, J.; Ruppert, A. M.; Matras-Michalska, J.; Jedrzejczyk, M.; Grams, J.; Sautet, P. *Chem. Commun.* **2014**, *50*, 12450–12453.
- (80) Loffreda, D.; Michel, C.; Delbecq, F.; Sautet, P. *J. Catal.* **2013**, *308*, 374–385.

Graphical Abstract

